ADVANCED ENGINEERING MATERIALS
www.aem-journal.com

Exploring Refinement Characteristics in FeTi–Cu$_x$ Composites: A Study of Localization and Abrasion Constraints

Lukas Schweiger, Florian Spieckermann,* Nadine Buchebner, Julius F. Keckes, Daniel Kiener, and Jürgen Eckert*

FeTi–Cu composites with varying Cu contents are subjected to high-pressure torsion, and their deformation behavior is explored systematically using scanning electron microscopy, microhardness, and nanoindentation. The study identifies the limiting factors influencing the refinement during severe plastic deformation. The pronounced strength differences between phases lead to fragmentation primarily through hard–hard (FeTi–FeTi) contact points, promoted by homogeneous, i.e., nonlocalized, and possibly turbulent material flow. These conditions are prevalent in Cu-rich composites and during high-temperature deformation. Conversely, Cu-lean composites exhibit deformation localization, hindering the fragmentation process. Abrasion becomes an efficient refinement mechanism at the submicron-/nanoscale, particularly for composites containing higher concentrations of nanocrystalline FeTi and exhibiting homogeneous plastic deformation. Consequently, deformation localization in Cu-lean composites inhibits both refinement mechanisms, while Cu-rich compositions and higher temperatures result in efficient refinement but at the risk of coarsening at the nanoscale. Refinement is localization-limited in the former case and abrasion-limited in the latter. Optimized processing conditions can overcome these constraints, yielding a uniform nanocomposite. This study sheds light on the intricate interplay of the mechanical properties of the respective phases in a composite, emphasizing the importance of tailored compositions and deformation conditions to optimize nanocomposites, particularly when dealing with challenging material pairings.

1. Introduction

High-pressure torsion (HPT) is a promising tool for creating nanocrystalline materials.[1,2] Above that, it proves versatile in creating intricate multiphase materials, nanocomposites,[3] supersaturated solid solutions,[4] and other metastable phases that are otherwise not accessible. Various processes have been reported, e.g., the deformation-induced crystallization of bulk metallic glasses,[5] that are otherwise not achievable with conventional deformation methods. Despite its apparent simplicity, as severe plastic deformation (SPD) is achieved by applying simple shear deformation under high pressures, HPT offers tremendous opportunities. However, many intricacies of the process are not yet fully understood.[6] These were thoroughly discussed in a recent review from Beygelzimer et al. and include, for example, the mechanisms of ideal plasticity, the related saturation behavior of the microstructure, the occurrence of solid-state turbulent plastic flow, and the nature of the anvil sample contact.[6]

Many materials obtainable by HPT, and in a broader sense SPD, possess attractive and superior mechanical and functional properties and might be vital in enabling technological advancement and the transition to a sustainable and green economy. Such materials encompass hard or soft magnetic materials,[7,8] materials with strength–ductility synergy,[9] with excellent fatigue resistance,[10] and materials for solid-state hydrogen storage.[11] The last example targets materials with enhanced hydrogen sorption properties, such as improved activation behavior, kinetics, and capacity.[12–15] Additionally, hydrogen storage materials that were not accessible otherwise were reported by synthesis/mechanical alloying using HPT.[16] One promising hydrogen storage material is FeTi,[17] as it has an excellent volumetric storage capacity,[18] contains abundant elements,[19] is potentially cheap,[20,21] and the possibility for preparing it from scrap has been reported in the literature.[22] Its biggest drawback, however, is that FeTi has sluggish initial hydrogen absorption and needs to be activated by an appropriate heat treatment under a hydrogen atmosphere at 450 °C.[23]

L. Schweiger, F. Spieckermann, N. Buchebner, J. F. Keckes, D. Kiener, J. Eckert
Department of Materials Science
Montanuniversität Leoben
Jahnstraße 12, 8700 Leoben, Austria
E-mail: lukas.schweiger@unileoben.ac.at; florian.spieckermann@unileoben.ac.at

J. Eckert
Erich Schmid Institute of Materials Science
Austrian Academy of Sciences
Jahnstraße 12, 8700 Leoben, Austria

The ORCID identification number(s) for the author(s) of this article can be found under https://doi.org/10.1002/adem.202400593.

DOI: 10.1002/adem.202400593

Several attempts were made to improve the activation behavior of FeTi, with alloying[24,25] and mechanical treatments being the most promising routes. The latter includes ball milling of FeTi[26–28] and its deformation utilizing HPT.[29,30] Although the HPT-deformed FeTi exhibited promising absorption properties,[29,31] the resulting microstructure was reported to be heterogeneous. As FeTi is an intermetallic with limited plasticity[32] and reported microhardness values of up to 10 GPa after HPT,[29] controlled microstructural engineering remains challenging but critical when considering the widespread usage of any material for engineering and functional applications.[33]

Consequently, we prepared FeTi–Cu composites with a targeted nanocrystalline structure, i.e., a metal–metal nanocomposite.[3] The Cu takes the role of a soft and ductile[34] supporting phase with limited miscibility with FeTi,[35,36] enabling controlled processing and the formation of a uniform micro- and nanostructure. Previously, we reported on the general difficulties associated with the deformation of such FeTi–Cu composites with 25 vol% Cu, highlighting that mainly deformation localization inhibits efficient refinement of the composite.[37] In this study, we expand the investigation on composites with varying Cu contents. The resulting microstructures are critically assessed and discussed with regard to some of the unresolved phenomena mentioned above, occurring during HPT. In particular, this study shows that different mechanisms promote refinement at the micro- and submicron-/nanoscale. Depending on the Cu content, the refinement behavior and consequent microstructural evolution of the composite are found to be localization-limited for Cu-lean composites, i.e., deformation localization inhibits fragmentation of FeTi particles, and abrasion-limited for Cu-rich composites, i.e., refinement by abrasion at the submicron-/nanoscale becomes inefficient, leading to a coarser nanocomposite.

2. Results and Discussion

2.1. Microstructural Characterization and Parameterization

The backscatter-electron (BSE) scanning electron microscopy (SEM) images in **Figure 1** show the microstructures of FeTi–Cu with a–c) 15 vol%, d–f) 25 vol%, g–i) 35 vol%, j–l) 42.5 vol%, and m–o) 50 vol% Cu. From top to bottom, the micrographs represent the compacted and the as-HPT states after room temperature (RT) and 400 °C (high temperature [HT]) deformation. The darker regions represent FeTi particles, while the brighter regions correspond to either Cu or the FeTi–Cu nanocomposite, where the individual phases of FeTi and Cu cannot be distinguished. All samples were deformed for 50 revolutions to ensure good sample homogeneity at higher disk radii (radius $\gg$ 0 mm). Figure 1p depicts an exemplary cross section of an HPT disk, representing the achievable degree of homogeneity, including the coarser microstructure unavoidable in the center. Figure 1 shows that the FeTi–Cu composites exhibit different microstructures depending on the temperature and the Cu fraction. In accordance with the previous literature, samples display a more homogeneous microstructure when deformed at HT. Higher deformation temperatures are beneficial for efficient refinement of the harder phase, e.g., in FeTi–Cu,[37] Fe–Mg,[38] W–Cu,[39] or Cu–Fe–Co.[40] This study confirms that high deformation temperature holds importance even when increasing the amount of Cu, i.e., the mechanically softer and more deformable phase.

The microstructures were assessed by quantifying the area fractions of the dark (FeTi) and bright areas (Cu or FeTi–Cu nanocomposite) of the micrographs at intermediate radii (3.5 mm $> r >$ 1 mm, amounting to an overall area of about 1.25 mm^2). This allows the determination of the amount of

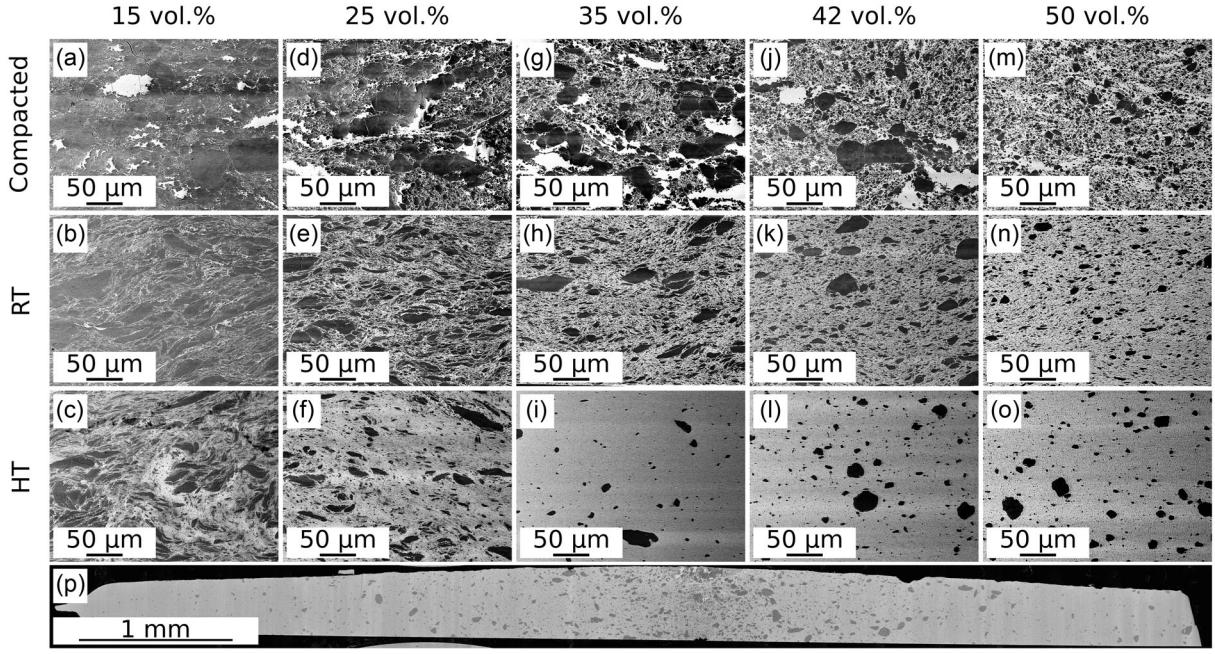

Figure 1. BSE SEM micrographs showing the microstructures at the micron-scale of FeTi–Cu composites with a–c) 15 vol% Cu, d–f) 25 vol% Cu, g–i) 35 vol% Cu, j–l) 42.5 vol% Cu, and m–o) 50 vol% Cu obtained before/after HPT deformation for 50 revolutions at RT and 400 °C (top to bottom). p) Complete cross section of an FeTi 35 vol% Cu composite deformed at 400 °C for 50 revolutions.

residual FeTi particles, which exceed the targeted nanocrystalline/ultrafine-grained (ufg) length scale (≥500 nm),[37] as shown in **Figure 2** and **3**. Residual FeTi, present under all processing conditions, is a reliable indicator of homogeneity and refinement efficiency, with a lower amount (area fraction, size, and number of particles) indicating a more homogeneous microstructure.

Figure 2a plots the area fraction of residual FeTi normalized to the nominal FeTi content in the composite. Samples with higher Cu content seem to be more refined after the initial ball milling step for the preparation of the powder blend. However, this effect is rather weak, with a residual FeTi fraction of 0.85 and 0.75 at low and high Cu fractions, respectively. A more pronounced decrease is observed for RT deformation, exhibiting less residual FeTi and, therefore, better refinement with increasing Cu content. This indicates that fragmentation of FeTi is more efficient for Cu-rich composites. This trend is even more evident in Figure 2b, plotting the FeTi area fraction as a function of radius/strain. For RT-deformed samples, fragmentation of FeTi proceeds at a very slow rate as a function of strain, but is slightly faster for higher Cu contents. However, Cu-rich composites seem to exhibit strong fragmentation initially. Nevertheless, high deformation temperatures, i.e., 400 °C, yield the most efficient refinement, nearly irrespective of the Cu content, confirming previous investigations.[37] Figure 2b confirms this and shows a high fragmentation rate, especially at the initial stages of deformation. The fragmentation rate then levels off at high strains and radii as the microstructure reaches saturation. Only the most Cu-lean composites, i.e., 15 vol% Cu, remain unrefined even at elevated deformation temperatures. The lowest residual FeTi fraction was obtained for composites with intermediate Cu contents, i.e., 35 and 42.5 vol% Cu. At 50 vol% Cu, the differences between RT and HT deformation become less pronounced as the amount of residual FeTi of both states converges.

The particle size distributions for the compacted, RT-deformed, and HT-deformed states are depicted in Figure 3 in a double logarithmic fashion. This representation highlights the fractal distribution of the FeTi particles, typical for fragmentation processes.[37,41,42] As FeTi particles are fragmented during HPT deformation, the particle size distributions shift to lower particle counts and sizes. However, under all deformation conditions, the distributions converge to a maximum particle size in the range of 20–100 μm for high and low Cu fractions, respectively. This indicates that a few relatively large FeTi particles remain in the microstructure, irrespective of processing conditions. For better visualization, the filled area between the curves corresponding to the compacted and the HT-deformed states illustrates the refinement efficiency of HT deformation. It becomes evident that at intermediate Cu contents, i.e., 35 and 42.5 vol% Cu, FeTi particles are fragmented most effectively, aligning with the previous results from Figure 2.

Another striking feature of the distributions is that the differences between the compacted and RT-deformed states are relatively small compared to the changes after HT deformation, indicating minimal RT refinement. This discrepancy between Figure 2 and 3 arises because each particle analysis highlights different aspects of the microstructure. A lower area fraction in Figure 2 signifies that FeTi particles are refined below the residual FeTi detection limit, i.e., 500 nm. This continuous fragmentation of particles during HPT creates a fractal distribution, as shown in Figure 3. This ongoing fragmentation, potentially occurring even with a stable underlying particle size distribution, contributes to refinement but might not be captured in the distribution. In particular, larger particles are statistically hardly included in the particle size distributions in Figure 3 but contribute significantly to the representation in Figure 2. Nevertheless, the distribution is a reliable measure of overall microstructure similarity. In the cases of RT deformation, this highlights that some fragmentation takes place initially, but without any profound changes to the composite microstructure. A subtle difference is observable in Figure 3, with the right tail of the distributions shifting to smaller particle sizes with increasing Cu content. This is related to slight variations of the respective starting powders.

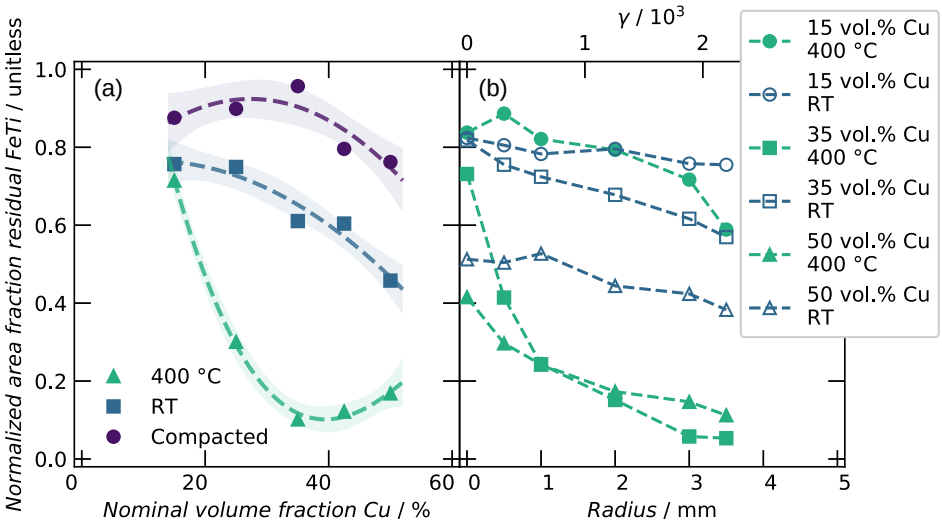

Figure 2. Area fraction of residual FeTi particles embedded in the Cu/FeTi–Cu matrix, normalized to the nominal FeTi fraction in the composite: a) as a function of Cu content (3.5 mm > r > 1 mm, $\gamma \approx 630$–2200, amounting to an overall area of about 1.25 mm^2, lines are added as guides to the eye) and b) as a function of radius/strain.

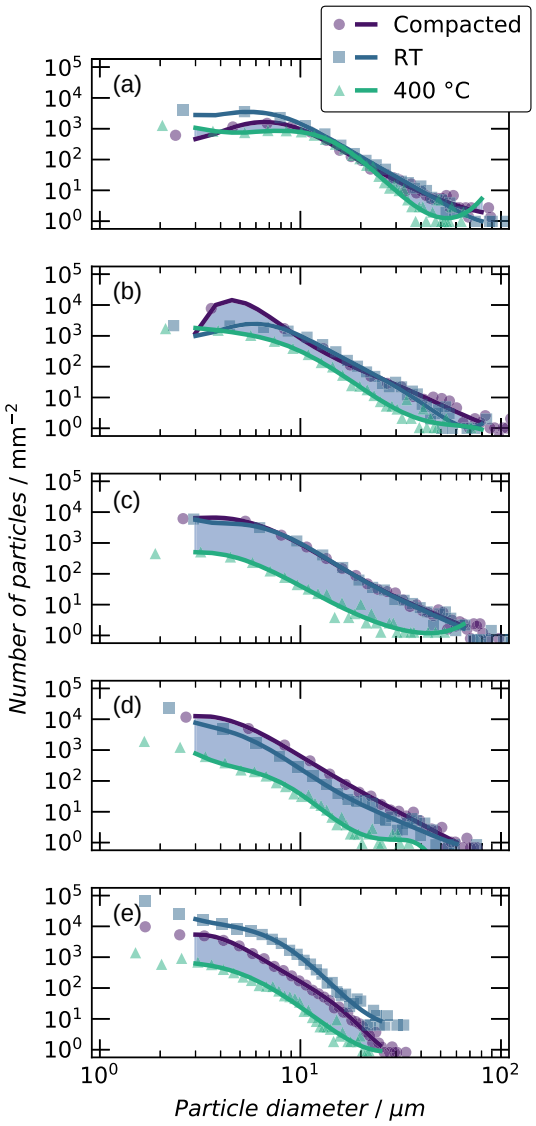

Figure 3. Particle size distributions of the compacted powder and samples deformed at RT and 400 °C for 50 revolutions ($3.5\,\text{mm} > r > 1\,\text{mm}$, $\gamma \approx 630$–2200) plotted in a double logarithmic fashion. The composites contain a) 15 vol%, b) 25 vol%, c) 35 vol%, d) 42.5 vol%, and e) 50 vol% Cu. Splines are added as guides to the eye.

As HT deformation allowed the formation of a homogenous nanocomposite, i.e., two interpenetrating phases, further characterization was devoted to these conditions. Higher resolution micrographs in **Figure 4** complement the previous results. The Cu-rich composites, i.e., 42.5 and 50 vol% Cu, exhibit poor homogeneity at the submicron-/nanoscale. On the contrary, samples with a Cu content of 35 vol% Cu have a uniform nanocomposite matrix. Cu-lean composites, including 15 and 25 vol%, again exhibit a more heterogeneous structure with bright, presumably Cu-rich, bands in which deformation localization can occur.[37] These results confirm that the microstructure is most homogenous at intermediate Cu contents of about 35 vol% Cu. However, for the Cu-rich variants, the relatively poor homogeneity at the submicron-/nanoscale differs from the microscale results, implying different material behavior during HPT at different length scales. The micron-scale refers to the composite structure at a length scale of about 10–1000 µm, as represented in Figure 1, while the submicron-/nanoscale denotes the nanocomposite structure around and below 1 µm, as represented by **Figure** 4 and **5**.

Additional high-resolution SEM images of the nanocomposite matrix were taken to evaluate the respective particle sizes. Figure 5a shows a BSE micrograph of a sample deformed at RT, indicating that FeTi was not sufficiently fragmented to form a nanocomposite. Instead, the structure consists of submicron-scaled FeTi particles embedded in a Cu matrix. Only HT deformation results in a nanocomposite, as displayed in Figure 5b–e, together with the corresponding particle sizes in Figure 5f. For 25 and 35 vol% Cu composites, the nanoscale FeTi forms a continuous network, while composites with 42.5 and 50 vol% Cu contain an apparent Cu matrix phase. Figure 5f indicates that the finest nanocomposites, with particle sizes of ≈25 nm, are achieved with 35–42.5 vol% Cu, suggesting that this ratio is optimal for refinement and subsequent nanocomposite formation. Despite the use of a watershed algorithm during analysis, the distributions for the continuous particle networks in Figure 5b,c are associated with an increased error, as reflected by the larger error bars in Figure 5f.

In addition to the fragmentation, the refinement of the composites also induces mechanical alloying, which was determined and discussed in a previous study on FeTi 25 vol% Cu composites.[37] Only the efficient refinement by HT deformation induced appreciable mechanical alloying of Cu in FeTi and vice versa. Consequently, it was concluded that mechanical alloying might support but not induce fragmentation of FeTi particles. Up to 4 at% Cu dissolved in FeTi and up to 6 at% (Fe + Ti) in Cu at a deformation temperature of 400 °C and 50 revolutions. A similar trend is expected for other Cu contents in this investigation.

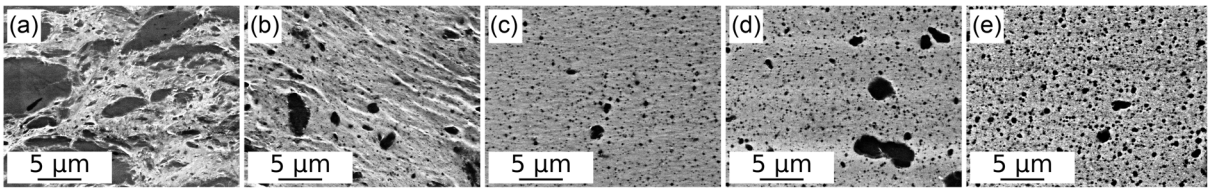

Figure 4. BSE SEM micrographs showing the microstructure in the micron- to submicron-range of FeTi–Cu composites with a) 15 vol%, b) 25 vol%, c) 35 vol% d) 42.5 vol%, and e) 50 vol% Cu obtained after HPT deformation at 400 °C for 50 revolutions ($r = 3\,\text{mm}/\gamma \approx 1900$).

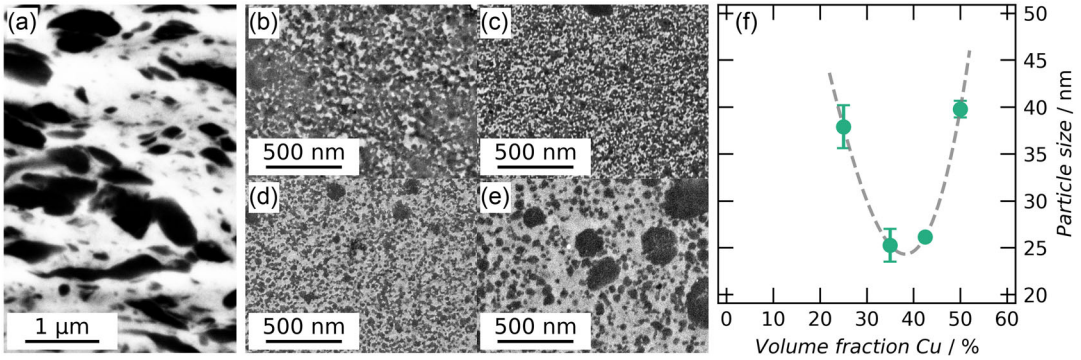

Figure 5. a) High-resolution BSE SEM micrograph of a composite with 35 vol% Cu deformed at RT for 50 revolutions. In-lens SEM images at high magnification representing the submicron-/nanoscale structure of composites deformed at 400 °C containing b) 25 vol%, c) 35 vol%, d) 42.5 vol%, and e) 50 vol% Cu, and f) the determined particle sizes plotted as a function of the Cu volume fraction. Micrographs were taken at $r = 3$ ($\gamma \approx 1900$).

2.2. Mechanical Properties—Global and Local

Vickers microhardness measurements were performed along the cross section of the HPT disk to probe the mechanical properties, with the results plotted in **Figure 6**a as a function of the introduced strain. All samples showed a distinct hardness trend, being harder at higher strains γ and arriving at a steady-state hardness above a certain strain. This saturation phenomenon was most pronounced for HT deformation and is commonly observed during HPT.[6] As visible in Figure 6a, the FeTi–Cu composites exhibit saturation and, with increasing Cu contents, progressively more defined hardness plateaus. At 25 vol% Cu, a slight hardness gradient is still visible after 50 revolutions. This less distinct hardness plateau and the relatively large standard deviations indicate a limited microstructural refinement and consequent saturation. This is even more pronounced for the 15 vol% Cu samples, with the microhardness not changing within the error margins for any of the composite states, confirming that little to no microstructural refinement occurred.

Figure 6b shows that the average hardness decreases with increasing Cu content, as it is the mechanically softer phase compared to FeTi. The reported hardness is 2–3 GPa[43–46] for Cu and 5–10 GPa for FeTi, respectively.[29,47] Additionally, the microhardness variance is a measure of microstructural homogeneity.[37] Under all processing conditions, higher Cu contents clearly show a much lower standard deviation in Figure 6b, indicating higher homogeneity of the structure at the rather large length scale (30–40 µm) probed during microhardness measurements. However, this cannot be extrapolated to the submicron-/nanoscale. The coarser structure of Cu-rich composites at this scale, visible in Figure 4d,e and 5d,e, is therefore not captured by this standard deviation.

The hard-to-soft phase ratio primarily determines the resulting hardness, with higher Cu contents lowering the hardness. None of the nanocomposites obtained in this series resulted in hardness values exceeding that of the harder phase, i.e., FeTi. Such strength synergies are often observed for systems subjected to SPD, e.g., Cu–Ta,[48] Cu–Nb,[49] and Al–Ti.[50] Overall, HT deformation results in a higher hardness,

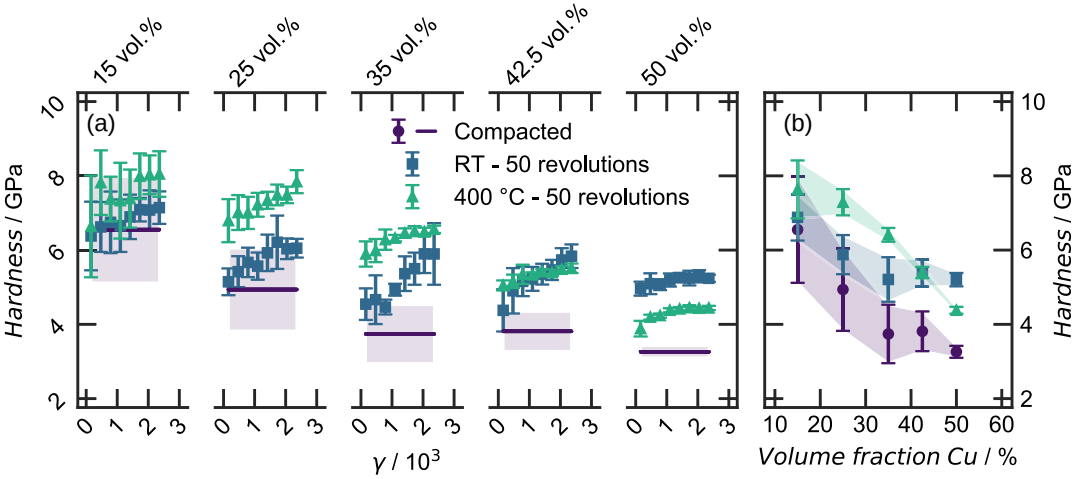

Figure 6. a) Vickers microhardness measurements of samples with various Cu contents as a function of the nominally introduced shear strain; markers are colored according to the deformation temperature. b) The average microhardness values at a radius between 3.5 and 1 mm ($\gamma \approx 630$–2200) are plotted as a function of the Cu content.

presumably due to the intensified fragmentation and consequent Hall–Petch strengthening. A notable feature is that the hardness of Cu-rich composites with 42 vol% Cu and 50 vol% Cu after RT deformation equals and exceeds the hardness after HT deformation, respectively. The origin of this is likely related to recovery/recrystallization phenomena occurring in the Cu phase during HT but not RT deformation.

Nanoindentation was performed to probe the local mechanical properties of the composite with 25 vol% Cu in detail, complementarily to the microhardness. As shown in Figure 1 and 6, this composite exhibited a significant difference in microstructure and hardness between RT and HT deformation and, therefore, was best suited to investigate the origins of the underlying refinement mechanisms.

Figure 7a depicts the RT hardness measured after RT deformation, with the corresponding map overlaid on the SEM micrograph. It confirms that the composite exhibits large differences in hardness, with FeTi particles/FeTi-rich regions being harder than Cu-rich regions. The continuous changes are clearly related to the distribution of FeTi and Cu. The vast range of mechanical hardness is additionally highlighted in Figure 7b. Figure 7b plots the hardness against the reduced modulus of both the RT- and HT-deformed samples, the latter of which was tested at both RT and 400 °C, respectively. The upper part of the cluster obtained from the RT-deformed sample by RT nanoindentation can be associated with larger FeTi particles. The upper bound of the reduced modulus was converted to the Young's modulus using the Poisson ratio of bulk FeTi ($\nu_{\mathrm{FeTi}} = 0.29$, $\nu_{\mathrm{Diamond}} = 0.07$, $E_{\mathrm{Diamond}} = 1140$ GPa).[51,52] The obtained Young's modulus is 260 GPa and slightly overestimates the value of 236 GPa calculated for FeTi using DFT and the Voigt–Reuss–Hill approximation.[51] The measured hardness values of up to 18 GPa far exceed those determined by microhardness. As FeTi is a highly brittle material prone to cracking, we conclude that previous results based on microhardness might underestimate the hardness of FeTi.[29,37] Cracking is also visible in Figure 7a, indicating that even nanoindentation might underestimate the average hardness of FeTi. Other studies performed nanoindentation on FeTi confirm values ranging from 12[53] to 19 GPa.[54]

Nevertheless, most hardness values cluster in the range of 5–10 GPa and 180–220 GPa for the hardness and reduced modulus, respectively. These values are associated with the Cu matrix containing dispersed FeTi, i.e., the FeTi–Cu composite matrix. It can be assumed that all compositions with higher Cu contents should exhibit even lower hardness values and, thereby, a more significant hardness difference between the FeTi–Cu composite matrix and residual FeTi particles. The expected Young's modulus for the nanocomposite ranges from 195 to 206 GPa, based on the models of Voigt and Reuss,[55] respectively, aligning with the estimated mean of the RT-deformed FeTi–Cu composite.

As the composites processed by HT deformation have a relatively homogeneous microstructure, only the nanocomposite matrix was probed. It exhibited a strongly reduced hardness of 4.1 ± 0.5 GPa at 400 °C compared to 11.3 ± 1.0 GPa at RT. Due to the high degree of nanocomposite homogeneity, as visible in Figure 7b, the samples deformed at HT exhibit a much narrower spread in modulus and hardness. Notably, the modulus of HT-deformed samples decreases, likely due to a significant fraction of atoms at grain and phase boundaries, weakening the average bond strength. Modeling the evolution of the modulus with temperature based on data from Chang et al.[56] and Zhu et al.[57] suggests a further decrease of up to 29–34 GPa (15%–17%) with increasing temperature. Our experiments roughly match the expected decrease in the FeTi–Cu nanocomposite's modulus. In fact, the observed decrease is slightly larger (42 GPa and 31%), possibly due to nonequilibrium grain and phase boundaries.

By varying the indentation strain rate for both RT and HT testing, as depicted in **Figure 8**, the strain-rate sensitivity (SRS) of the composites was estimated. The results for RT testing showed minor hardness changes, both after RT and HT deformation. RT-deformed samples exhibited a negligible SRS of -0.007 ± 0.029, while HT-deformed samples showed an elevated SRS of 0.034 ± 0.026, albeit with a notable standard

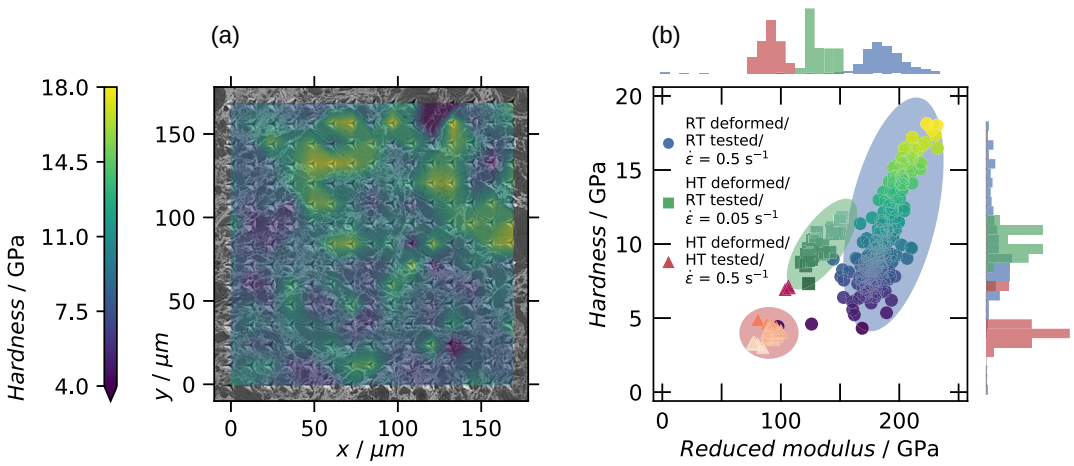

Figure 7. Nanoindentation measurements a) of the RT-deformed sample at RT with the SEM image (SE detector) of the indent array overlaid with the hardness map. b) Scatter plot of the hardness and reduced modulus of samples deformed at RT and HT; the HT sample was tested at both RT (RT tested) and 400 °C (HT tested). All measurements were performed on FeTi 25 vol% Cu composites.

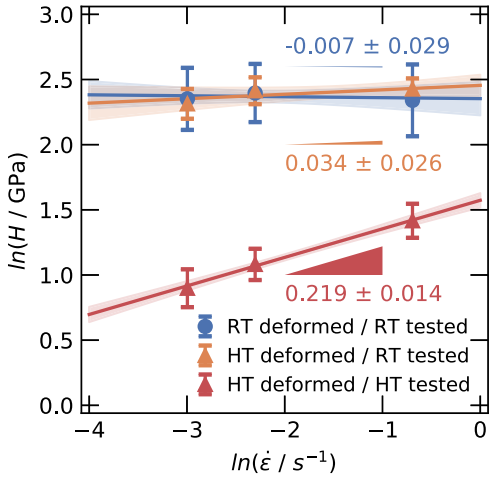

Figure 8. Evaluation of the SRS by nanoindentation measurements at various strain rates, with the slope of the weighted linear regression corresponding to the SRS parameter *m*.

deviation. Previous studies report a minor SRS of 0.004 for FeTi[53] and moderate values of 0.02–0.06 for ufg to nanocrystalline Cu,[46,58] the latter showing higher SRS values at smaller grain sizes. The weighted averages, derived from the aforementioned values, are 0.008 and 0.018 when considering the lower and upper SRS values of Cu, respectively. These values qualitatively align with the RT results of the coarser (ufg) RT-deformed composite and the more refined (nanocrystalline) HT-deformed composite. The high standard deviation might be imparted due to the different SRS behavior of the respective phases. At 400 °C, however, the nanocrystalline composite obtained by HT deformation demonstrates a significant SRS of 0.219 ± 0.014. Such a drastic increase of the SRS with temperature is in line with previous observations on Cu–Nb nanocomposites, with reported values of 0.106 at 400 °C[59] and 0.35/0.51 at 700 °C.[49] Also, Cu–Co nanocomposites exhibited an enhanced SRS of 0.045 at RT,[60] while, on the other hand, Cu–W composites show a comparably low SRS of about 0.07 at 400 °C.[61] This enormous increase of the SRS is in line with a previously proposed mechanism for the refinement of metal–metal composites, suggesting efficient refinement to be due to the increase of the SRS of the ufg/nanocrystalline Cu and consequent FeTi–Cu nanocomposite at elevated temperatures.[37]

2.3. Cu-Lean Composites—Localization Limited Refinement

Figure 2, 3, and 6 show that neither RT nor HT deformation causes fragmentation of FeTi in composites containing only 15 vol% Cu. These composites maintain an unchanged residual FeTi volume fraction, particle size, and hardness distribution. Additionally, the high standard deviation of the latter indicates a heterogeneous microstructure and significant hardness difference between the respective phases. Therefore, Cu-lean compositions do not result in any meaningful refinement of FeTi particles, regardless of the conditions. Figure 1 confirms that these composites remain heterogeneous and coarse-grained. A closer investigation of the microstructure, as shown in

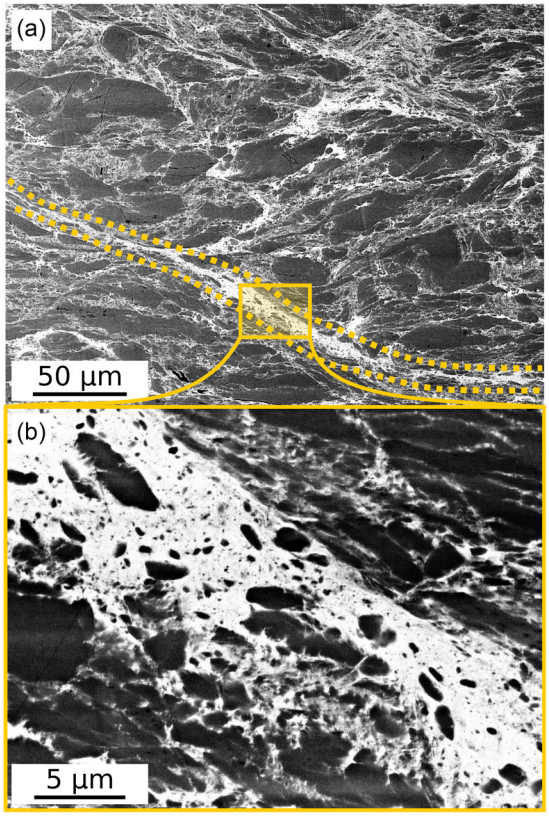

Figure 9. BSE SEM micrographs of FeTi 15 vol% Cu samples deformed at 400 °C for 50 revolutions at a radius of 2 mm ($\gamma \approx 1257$). The marked region in a) constitutes a Cu-rich band, shown magnified in b).

Figure 9a, reveals Cu bands in the composite after HT deformation. As Cu is the softer and more deformable phase compared to FeTi,[29,43–45,47] such bands will carry most deformation during HPT. RT nanoindentation measurements shown in Figure 7b confirmed the significant differences in mechanical properties of the Cu-rich matrix and residual FeTi particles, with the latter having a hardness of up to 18 GPa, in the literature, even up to 19 GPa.[54] Consequently, if strain hardening and strain-rate hardening are insufficient, deformation persists within these narrow Cu bands.

Overall, the above results show that refinement in Cu-lean composites is localization-limited. The localized plastic flow inhibits the fragmentation process, and therefore, no saturation of the microstructure and associated mechanical properties, e.g., hardness, is achieved. In this localization-limited case, the microstructure is determined by the mechanical properties and the resulting plastic flow. Under these conditions, the evolution of the microstructure should be sensitive to the original distribution of the constituent phases. This starkly contrasts the model of an equifinal state after HPT, as proposed by Straumal et al.[62] This model postulates that, within certain boundaries, HPT of a specific chemical composition results in a certain structural state, irrespective of the starting configuration, e.g., supersaturated solid solution or two-phase material.[62–66] Nevertheless, the conclusions drawn above do not necessarily conflict with the

equifinal model for HPT deformation. They rather introduce an additional requirement, particularly in the case of immiscible systems: homogeneous or ideal plastic deformation. This entails preventing deformation localization, thereby facilitating the fragmentation essential for establishing equifinal and steady-state conditions.[67]

2.4. Cu-Rich Composites—Homogenous Deformation and Abrasion-Limited Refinement

As shown in Figure 2 and 3, increasing the Cu content above the percolation threshold[68] (about 20 vol% Cu under the assumption of a random phase distribution) results in better refinement by HPT, both at RT and HT. However, only HT deformation provides the targeted homogenous nanocomposite, i.e., two interpenetrating phases, while RT deformation yields a comparable coarse composite, as shown in Figure 1 and exemplified in Figure 5a.

Cu[43–45] is mechanically softer compared to FeTi,[29,47] and FeTi exhibits limited plastic deformability at the investigated processing conditions.[32] This is supported by Figure 6, which illustrates that the hardness of FeTi–Cu composites decreases with increasing Cu content. Consequently, the strength difference between the larger FeTi particles and the respective matrix increases, and the fracture of the harder residual FeTi particles should become more difficult for a Cu-rich (nano)composite matrix. With this consideration, achieving efficient refinement in such composites would necessitate significant strength synergy, wherein the nanocomposite matrix has a hardness exceeding that of the individual coarse-grained materials. While examples of such strength synergy have been reported, such as in the Cu–Ta system,[48] it is not observed in the current FeTi–Cu system. Therefore, as discussed in the literature for composites combining soft and hard phases, hard–hard, i.e., FeTi–FeTi, contact points are essential to induce fragmentation of FeTi particles.[4] However, the observation of improved refinement for higher Cu contents is still an a priori paradox, as one might expect better refinement at higher FeTi contents due to the higher probability of hard–hard contact points promoting the fracture of such particles.

However, the above paradox can be resolved when considering that, as the Cu content increases, the composite becomes more deformable and less prone to localized deformation.[69–71] The plastic flow within the matrix becomes more evenly distributed, and the dispersed FeTi particles are dragged along. Under these conditions, the mean distance covered by the FeTi particles increases, and collisions and particle arrangements that promote fracture become more frequent. Additionally, all investigated composites contain a relatively high amount of FeTi phase, blocking unhindered shear deformation of the Cu, possibly leading to turbulent flow.[72] Although not common in solids, turbulent flow has been reported for HPT[6,73,74] and is also associated with efficient refinement of multiphase laminates.[72,75] Therefore, these processes might also be crucial for the efficient fragmentation of FeTi particles.

In contrast, if most of the deformation is localized in narrow bands, as illustrated in the counterexample in Figure 9, the movement of most FeTi particles during deformation is limited. Consequently, the particles will remain surrounded by a Cu shell and not come into contact with other FeTi particles. In such scenarios, present in Cu-lean composites, many potential hard–hard contact points promoting fracture are theoretically possible, but not realized due to the narrow deformation bands. As a result, the high FeTi content cannot effectively contribute to fracture and subsequent refinement.

The above considerations highlight that 1) efficient fragmentation in a composite such as FeTi–Cu occurs when hard–hard contacts (FeTi–FeTi) induce stress states leading to fracture and that 2) more homogeneous deformation promotes the frequency of such events. Therefore, to enable efficient refinement, the plastic flow must be distributed homogenously throughout the HPT cross section, avoiding deformation localization. Such deformation localization can be suppressed by either strain hardening or strain-rate hardening.[76–78] Strain hardening originates from the increase in dislocation density,[79] transformation-induced plasticity,[80] or twinning-inducted plasticity[81] effects, and strain-rate hardening from the rate dependence of thermally activated deformation processes.[82] The potential for strain hardening in a nanocrystalline material in saturation is negligible, and consequently, only a pronounced strain-rate hardening response can suppress localization and support the uniform distribution of plastic strain.[77,78] Such a pronounced strain-rate hardening response is typically characterized by a large value of the SRS. Higher deformation temperatures increase the SRS of nanocrystalline Cu, as well as ufg bcc metals.[83–85] High SRS values are also reported for intermetallics at elevated temperatures.[86] Consequently, the SRS of the overall (nano) composite should increase with temperature. This increase was confirmed by nanoindentation presented in Figure 8, showing a drastic increase of the SRS from 0.034 ± 0.026 at RT to 0.219 ± 0.014 at 400 °C. Both values amount to an activation volume of 2.4 ± 2.1 and $3.3 \pm 0.6\ b^3$, respectively. The high SRS values and the single digit activation volumes indicate grain boundary-mediated deformation processes[87,88] with strong diffusional contributions.[89–91] Based on the above arguments, this SRS increase promotes homogeneous deformation and, therefore, refinement, aligning with the observations that HT deformation results in nanocomposite formation and a more uniform microstructure. Nevertheless, although the resulting plastic flow of the nanocomposite is homogenous at the mesoscale, the deformation is localized at the nanoscale, most likely at grain and phase boundaries.

Therefore, the synergistic presence of high deformation temperatures and high Cu contents allow the facile fragmentation of FeTi particles due to a reduced deformation localization tendency, escaping the localization-limited deformation region. However, the high-magnification micrographs in Figure 4 and 5 show that the nanocomposites obtained by HT deformation have a distinct particle size minimum at intermediate Cu contents, i.e., 35 and 42.5 vol% Cu. This disparity between the microscale and submicron-/nanoscale demonstrates that different refinement mechanisms are dominant at different length scales, which is in line with other studies pointing out the multifractal behavior of composites during HPT.[42]

A possible explanation would be that small particles are not refined by fracture but by abrasion, i.e., the continuous removal of material from larger FeTi particles by the plastic flow of

the surrounding FeTi–Cu nanocomposite matrix. With both mechanisms active, the smaller the particles, the higher the relative contribution of abrasive refinement. However, this mechanism is ineffective in breaking larger FeTi particles down to the nanoscale. Instead, it results only in a rounder shape of the particles,[92] as observed in Figure 1i,l,o and 4c–e. In contrast, refinement at the nanoscale proceeds less by the mechanical fracture during deformation, but by the continuing abrasion/dissolution, potentially followed by reprecipitation. This scenario would result in a steady-state nanostructure and could be considered stationary or equifinal.[62]

Efficient abrasion should, therefore, be promoted by homogenously distributed and turbulent material flow, avoiding localization and shear band formation, coupled with a substantial concentration of hard and abrasive FeTi particles. Based on Figure 4 and 5, these prerequisites are fulfilled in composites with intermediate Cu contents, i.e., 35 and 42 vol% Cu, as these exhibit the minimum particle size at the submicron-/nanoscale. These composites do not suffer from localization while retaining elevated levels of FeTi. Nevertheless, this mechanism requires a minimal amount of FeTi in the composite to obtain a fine-scaled, homogenous nanocomposite by abrasion. If this condition is not met, the composite becomes coarser at the submicron-/nanoscale and might be considered to be in an abrasion-limited refinement regime. Figure 5e shows this is already the case for Cu-rich composites containing 50 vol% Cu.

Consequently, one can conclude that a homogenous nanocomposite forms if the localization and abrasion limitations determining the refinement at the microscale and submicron-/nanoscale are avoided. In FeTi–Cu composites, such optimum seems to be achieved at about 35 vol% Cu. The resulting nanocomposite might then be regarded as the most refined state achievable without any limitations inherent to the heterogeneous plastic flow of multiphase, complex materials during HPT. The mechanisms and limitations are illustrated in **Figure 10**.

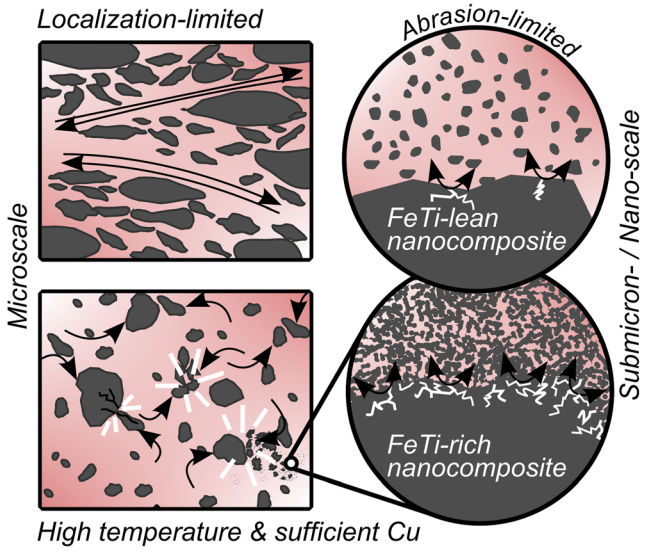

Figure 10. Illustration of the mechanisms responsible for the refinement of the FeTi–Cu composite at the micro- and the submicron-/nanoscale and the associated constraints and limitations.

3. Conclusion

In this study, FeTi–Cu composites with varying Cu contents were deformed by HPT, followed by extensive characterization using SEM, microhardness, and nanoindentation to investigate the mechanisms governing the refinement behavior and the formation of a homogeneous nanocomposite. Two mechanisms and their associated constraints were identified, both impacting the refinement of the harder FeTi phase during SPD.

First, due to the strength differences between the phases, the fragmentation of larger FeTi particles primarily occurs through hard–hard contact points between them. Higher Cu volume fractions and temperatures promote a more homogeneous and possibly turbulent material flow, aiding fragmentation. Conversely, Cu-lean composites exhibit deformation localization, hindering fragmentation.

The second mechanism, abrasion, primarily refines particles at the submicron-/nanoscale and is particularly effective in composites with higher nanocrystalline FeTi content. Again, this process benefits from homogeneous plastic deformation.

These observations lead to the identification of two refinement-limiting scenarios. 1) Pronounced deformation localization in Cu-lean composites, i.e., with 15 vol% Cu, hampers FeTi particle fracture and renders abrasion inefficient. Refinement is *localization-limited*. 2) At HT and higher Cu content, deformation is distributed evenly and, coupled with turbulent flow, leads to frequent fracturing and efficient refinement of FeTi. However, with more Cu, the abrasive effect becomes weaker, and the resultant composite remains relatively coarser at the submicron-/nanoscale. Refinement is *abrasion-limited*.

Optimized compositions and deformation conditions, i.e., 35 vol% Cu and HT deformation at 400 °C, avoid these constraints and result in a homogenous and uniform nanocomposite.

In revealing the crucial interplay of hard–hard contacts and abrasion in the deformation behavior of FeTi–Cu composites, this study emphasizes the importance of carefully tailored compositions and deformation conditions for the achievement of homogeneous refinement. Additionally, it offers insight necessary for the optimization of nanocomposites of challenging material pairings with promising functional properties.

4. Experimental Section

Sample preparation: FeTi was produced using an arc melter (Arc Melter AM 0.5, Edmund Bühler GmbH, Germany) with Fe flakes (99.99+%, HMW Hauner GmbH, Germany) and Ti granules (99.995%, HMW Hauner GmbH, Germany) in stoichiometric amounts. The resulting ingot was crushed using mortar and pestle. Ball milling was performed to ensure the uniformity of the FeTi–Cu powder blend. The powder was compacted under an inert gas atmosphere and deformed at RT and 400 °C for 50 revolutions with a rotational speed of 1.23 rpm and a pressure of 7.5 (RT) and 6 GPa (400 °C), respectively. The details of the sample preparation are reported elsewhere.[37]

The shear strain γ introduced by HPT at a specific radius r was estimated based on the expression[93]

$$\gamma = \frac{2\pi n r}{t} \quad (1)$$

with n being the number of revolutions and t the thickness of the sample. After HPT deformation, the samples had a thickness of about 0.5 mm.

Microstructural characterization: The HPT disks were cut in half and mirror-polished to enable a complete cross-sectional investigation of the microstructure by SEM (LEO type 1525, Carl Zeiss GmbH, Germany). For parameterization (area fractions, particle analysis), the software packages Ilastik[94] (Version 1.3.3), Fiji (Version 1.53)[95] (including the BioVoxxel plugin[96]), as well as a Python 3.9 script including packages such as OpenCV[97] (Version 4.5.4.58), Scikit-Image[98] (Version 0.18.1), and Scipy[99] (version 1.6.2) were used. In order to ensure reliable results, particularly for the larger FeTi contents and interconnected nanocomposites, watershed processing was used to separate the individual FeTi particles.

Mechanical characterization: The Vickers microhardness was measured using an universal laboratory hardness tester (DuraScan, ZwickRoell GmbH, Germany) on the polished cross sections prepared previously for SEM investigations. The load was 4.903 N ($HV_{0.5}$), and the load times and dwell times during the measurement were 6 and 10 s, respectively.

For local and higher resolved investigations, nanoindentation (FT-NMT04 IN-SITU SEM Nanoindenter, FemtoTools AG, Switzerland) was performed on the top side of the HPT disks at a radius of about 2–3 mm. The calibration was performed on fused silica. Depth-dependent hardness and reduced modulus were probed by using continuous stiffness measurements (100 Hz, 4 nm amplitude), and Berkovich tips made from diamond and tungsten carbide (HT measurements) were used. The reported hardness and reduced modulus data are derived from the depth-independent regions of the data. The experiments were performed using strain rate and displacement controlled indentations with indentation strain rates of 0.5, 0.1, and 0.05 s^{-1}. As the actual Poisson ratio of the composite is unknown, the reduced modulus is (mainly) reported. The activation volume was calculated with the equation

$$V^* = \frac{C\sqrt{3}\,k_b T}{m\,H} \tag{2}$$

with V^* being the activation volume, C the constraint factor set to 2.8, k_b the Boltzmann constant, T the temperature in K, m the SRS, and H the hardness. V^* is normalized by the mean Burgers vector of both FeTi and Cu.

Acknowledgements

This research activity is part of the Strategic Core Research Area SCoRe A + Hydrogen and Carbon and has received funding from Montanuniversität Leoben. The authors acknowledge the financial support of the European Research Council (ERC) under the European Union's Horizon 2020 research and innovation program (grant no. 771146 TOUGHIT).

Conflict of Interest

The authors declare no conflict of interest.

Data Availability Statement

The data that support the findings of this study are available from the corresponding author upon reasonable request.

Keywords

deformation localization, high-pressure torsion, mechanical properties, nanocomposites, refinement

Received: March 6, 2024
Revised: June 5, 2024
Published online: June 20, 2024

[1] R. Z. Valiev, Y. Estrin, Z. Horita, T. G. Langdon, M. J. Zehetbauer, Y. Zhu, *JOM* **2016**, *68*, 1216.
[2] R. Z. Valiev, Y. Estrin, Z. Horita, T. G. Langdon, M. J. Zehetbauer, Y. T. Zhu, *Mater. Res. Lett.* **2016**, *4*, 1.
[3] A. Bachmaier, R. Pippan, *Int. Mater. Rev.* **2013**, *58*, 41.
[4] K. S. Kormout, R. Pippan, A. Bachmaier, *Adv. Eng. Mater.* **2017**, *19*, 1600675.
[5] M. Antoni, F. Spieckermann, N. Plutta, C. Gammer, M. Kapp, P. Ramasamy, C. Polak, R. Pippan, M. J. Zehetbauer, J. Eckert, *Materials* **2023**, *16*, 1260.
[6] Y. Beygelzimer, Y. Estrin, R. Kulagin, *Mater. Trans.* **2023**, *64*, 1856.
[7] L. Weissitsch, F. Staab, K. Durst, A. Bachmaier, *Mater. Trans.* **2023**, *64*, 1537.
[8] G. Abrosimova, A. Aronin, D. Matveev, E. Pershina, *Mater. Lett.* **2013**, *97*, 15.
[9] R. Z. Valiev, I. V. Alexandrov, Y. T. Zhu, T. C. Lowe, *J. Mater. Res.* **2002**, *17*, 5.
[10] F. Kümmel, H. W. Höppel, M. Göken, *Adv. Eng. Mater.* **2021**, *23*, 2100070.
[11] K. Edalati, E. Akiba, Z. Horita, *Sci. Technol. Adv. Mater.* **2018**, *19*, 185.
[12] N. Klopčič, I. Grimmer, F. Winkler, M. Sartory, A. Trattner, *J. Energy Storage* **2023**, *72*, 108456.
[13] C. Weidenthaler, M. Felderhoff, *Energy Environ. Sci.* **2011**, *4*, 2495.
[14] J. Ren, N. M. Musyoka, H. W. Langmi, M. Mathe, S. Liao, *Int. J. Hydrogen Energy* **2017**, *42*, 289.
[15] Q. Lai, Y. Sun, T. Wang, P. Modi, C. Cazorla, U. B. Demirci, J. R. Ares Fernandez, F. Leardini, K. F. Aguey-Zinsou, *Adv. Sustain. Syst.* **2019**, *3*, 1.
[16] Á. Révész, M. Gajdics, *Energies* **2021**, *14*, 819.
[17] J. J. Reilly, R. H. Wiswall, *Inorg. Chem.* **1974**, *13*, 218.
[18] L. Schlapbach, A. Züttel, *Nature* **2001**, *414*, 353.
[19] G. K. Sujan, Z. Pan, H. Li, D. Liang, N. Alam, *Crit. Rev. Solid State Mater. Sci.* **2020**, *45*, 410.
[20] T. Tsuchiya, N. Yasuda, S. Sasaki, N. Okinaka, T. Akiyama, *Int. J. Hydrogen Energy* **2013**, *38*, 6681.
[21] M. Ma, D. Wang, X. Hu, X. Jin, G. Z. Chen, *Chem. Eur. J.* **2006**, *12*, 5075.
[22] Y. Shang, S. Liu, Z. Liang, F. Pyczak, Z. Lei, T. Heidenreich, A. Schökel, *Commun. Mater.* **2022**, *3*, 1.
[23] L. Schlapbach, T. Riesterer, *Appl. Phys. A Solids Surf.* **1983**, *32*, 169.
[24] J. R. Johnson, J. Reilly, in *Proc. Int. Conf. Altern. Energy Sources*, Upton, New York, NY **1977**, p. 3739.
[25] E. M. Dematteis, N. Berti, F. Cuevas, M. Latroche, M. Baricco, *Mater. Adv.* **2021**, *2*, 2524.
[26] H. Aoyagi, K. Aoki, T. Masumoto, *J. Alloys Compd.* **1995**, *231*, 804.
[27] H. Emami, K. Edalati, J. Matsuda, E. Akiba, Z. Horita, *Acta Mater.* **2015**, *88*, 190.
[28] A. K. Patel, D. Siemiaszko, J. Dworecka-Wójcik, M. Polański, *Int. J. Hydrogen Energy* **2022**, *47*, 5361.
[29] K. Edalati, J. Matsuda, H. Iwaoka, S. Toh, E. Akiba, Z. Horita, *Int. J. Hydrogen Energy* **2013**, *38*, 4622.
[30] K. Edalati, M. Matsuo, H. Emami, S. Itano, A. Alhamidi, A. Staykov, D. J. Smith, S. Orimo, E. Akiba, Z. Horita, *Scr. Mater.* **2016**, *124*, 108.
[31] K. Edalati, J. Matsuda, M. Arita, T. Daio, E. Akiba, Z. Horita, *Appl. Phys. Lett.* **2013**, *103*, 1.
[32] T. Suzuki, S. Uehara, in *Proc. Fourth Int. Conf. Titan.*, Metallurgical Society of AIME, Warrendale, PA **1980**, p. 1255.

[33] M. F. Ashby, D. R. H. Jones, in *Engineering Materials 2: An Introduction to Microstructures and Processing*, Butterworth-Heinemann, Oxford, UK **2013**.
[34] J. R. Davis, *ASM Speciality Handbook, Copper and Copper Alloys*, ASM International, Materials Park, OH **2001**.
[35] J. A. van Beek, A. A. Kodentsov, F. J. J. van Loo, *J. Alloys Compd.* **1995**, *217*, 97.
[36] V. Raghavan, *J. Phase Equilib.* **2002**, *23*, 172.
[37] L. Schweiger, D. Kiener, M. Burtscher, E. Schafler, G. Mori, F. Spieckermann, J. Eckert, *Mater. Today Adv.* **2023**, *20*, 100433.
[38] M. Roostaei, P. J. Uggowitzer, R. Pippan, O. Renk, *Scr. Mater.* **2023**, *230*, 115428.
[39] M. Wurmshuber, M. Burtscher, S. Doppermann, R. Bodlos, D. Scheiber, L. Romaner, D. Kiener, *Mater. Sci. Eng. A* **2022**, *857*, 144102.
[40] M. Stückler, L. Weissitsch, S. Wurster, H. Krenn, R. Pippan, A. Bachmaier, *J. Mater. Res. Technol.* **2021**, *12*, 1235.
[41] D. L. Turcotte, *J. Geophys. Res.* **1986**, *91*, 1921.
[42] I. Sabirov, R. Pippan, *Mater. Charact.* **2007**, *58*, 848.
[43] A. P. Zhilyaev, S. Swaminathan, A. A. Gimazov, T. R. McNelley, T. G. Langdon, *J. Mater. Sci.* **2008**, *43*, 7451.
[44] A. Abu-Oqail, A. Wagih, A. Fathy, O. Elkady, A. M. Kabeel, *Ceram. Int.* **2019**, *45*, 5866.
[45] H. Jiang, Y. T. Zhu, D. P. Butt, I. V. Alexandrov, T. C. Lowe, *Mater. Sci. Eng. A* **2000**, *290*, 128.
[46] J. Chen, L. Lu, K. Lu, *Scr. Mater.* **2006**, *54*, 1913.
[47] V. Zadorozhnyy, S. Klyamkin, M. Zadorozhnyy, O. Bermesheva, S. Kaloshkin, *Int. J. Hydrogen Energy* **2012**, *37*, 17131.
[48] N. Ibrahim, M. Peterlechner, F. Emeis, M. Wegner, S. V. Divinski, G. Wilde, *Mater. Sci. Eng. A* **2017**, *685*, 19.
[49] N. A. Mara, A. Misra, R. G. Hoagland, A. V. Sergueeva, T. Tamayo, P. Dickerson, A. K. Mukherjee, *Mater. Sci. Eng. A* **2008**, *493*, 274.
[50] C. Schunk, M. Nitschky, H. W. Höppel, M. Göken, *Adv. Eng. Mater.* **2019**, *21*, 1.
[51] K. Benyelloul, Y. Bouhadda, M. Bououdina, H. I. Faraoun, H. Aourag, L. Seddik, *Int. J. Hydrogen Energy* **2014**, *39*, 12667.
[52] A. Leitner, V. Maier-Kiener, D. Kiener, *Nanomaterials* **2018**, *8*, 366.
[53] T. Maity, B. Roy, J. Das, *Acta Mater.* **2015**, *97*, 170.
[54] Q. Chu, J. Li, X. W. Tong, S. Xu, M. Zhang, C. Yan, *Mater. Lett.* **2019**, *238*, 98.
[55] M. F. Ashby, in *Materials Selection in Mechanical Design*, Butterworth-Heinemann, Oxford, UK **2011**.
[56] Y. A. Chang, L. Himmel, *J. Appl. Phys.* **1966**, *37*, 3567.
[57] L. F. Zhu, M. Friák, A. Udyansky, D. Ma, A. Schlieter, U. Kühn, J. Eckert, J. Neugebauer, *Intermetallics* **2014**, *45*, 11.
[58] P. Huang, F. Wang, M. Xu, K. W. Xu, T. J. Lu, *Acta Mater.* **2010**, *58*, 5196.
[59] M. M. Primorac, M. D. Abad, P. Hosemann, M. Kreuzeder, V. Maier, D. Kiener, *Mater. Sci. Eng. A* **2015**, *625*, 296.
[60] A. Bachmaier, G. B. Rathmayr, J. Schmauch, N. Schell, A. Stark, N. De Jonge, R. Pippan, *J. Mater. Res.* **2019**, *34*, 58.
[61] M. Burtscher, M. Zhao, J. Kappacher, A. Leitner, M. Wurmshuber, M. Pfeifenberger, V. Maier-Kiener, D. Kiener, *Nanomaterials* **2021**, *11*, 1.
[62] B. B. Straumal, A. R. Kilmametov, B. Baretzky, O. A. Kogtenkova, P. B. Straumal, L. Lityńska-Dobrzyńska, R. Chulist, A. Korneva, P. Zięba, *Acta Mater.* **2020**, *195*, 184.
[63] B. B. Straumal, A. R. Kilmametov, Y. Ivanisenko, L. Kurmanaeva, B. Baretzky, Y. O. Kucheev, P. Zięba, A. Korneva, D. A. Molodov, *Mater. Lett.* **2014**, *118*, 111.
[64] B. B. Straumal, A. R. Kilmametov, I. A. Mazilkin, A. Korneva, P. Zieba, B. Baretzky, *JETP Lett.* **2019**, *110*, 624.
[65] B. B. Straumal, V. Pontikis, A. R. Kilmametov, A. A. Mazilkin, S. V. Dobatkin, B. Baretzky, *Acta Mater.* **2017**, *122*, 60.
[66] B. B. Straumal, A. R. Kilmametov, A. Korneva, A. A. Mazilkin, P. B. Straumal, P. Zięba, B. Baretzky, *J. Alloys Compd.* **2017**, *707*, 20.
[67] B. B. Straumal, R. Kulagin, L. Klinger, E. Rabkin, P. B. Straumal, O. A. Kogtenkova, B. Baretzky, *Materials* **2022**, *15*, 601.
[68] M. F. Ashby, in *Materials Selection in Mechanical Design*, Elsevier, Burlington **2011**, p. 341.
[69] I. L. Mogford, *Metall. Rev.* **1967**, *12*, 49.
[70] R. J. Arsenault, N. Shi, C. R. Feng, L. Wang, *Mater. Sci. Eng. A* **1991**, *131*, 55.
[71] J. W. Leggoe, A. A. Mammoli, M. B. Bush, X. Z. Hu, *Acta Mater.* **1998**, *46*, 6075.
[72] R. Kulagin, Y. Beygelzimer, Y. Ivanisenko, A. Mazilkin, B. Straumal, H. Hahn, *Mater. Lett.* **2018**, *222*, 172.
[73] Y. Beygelzimer, A. Filippov, Y. Estrin, *Philos. Mag.* **2023**, *103*, 1017.
[74] R. Kulagin, Y. Beygelzimer, Y. Ivanisenko, A. Mazilkin, H. Hahn, *IOP Conf. Ser. Mater. Sci. Eng.* **2017**, *194*, 012045.
[75] Y. Beygelzimer, Y. Estrin, A. Filippov, A. Mazilkin, M. Mail, B. Baretzky, R. Kulagin, *Mater. Lett.* **2022**, *324*, 132689.
[76] G. Gottstein, in *Physical Foundations of Materials Science*, Springer Berlin Heidelberg, Berlin, Heidelberg **2004**.
[77] E. Hart, *Acta Metall.* **1967**, *15*, 351.
[78] Y. M. Wang, E. Ma, *Mater. Sci. Eng. A* **2004**, *375–377*, 46.
[79] A. S. Argon, in *Strengthening Mechanisms in Crystal Plasticity*, Oxford University Press, New York, NY **2007**.
[80] W. Bleck, X. Guo, Y. Ma, *Steel Res. Int.* **2017**, *88*, 35.
[81] B. C. De Cooman, Y. Estrin, S. K. Kim, *Acta Mater.* **2018**, *142*, 283.
[82] V. Maier-Kiener, K. Durst, *JOM* **2017**, *69*, 2246.
[83] T. Suo, Y. Li, K. Xie, F. Zhao, K.-S. Zhang, Q. Deng, *Mech. Mater.* **2011**, *43*, 111.
[84] H. W. Höppel, J. May, M. Eisenlohr, M. Göken, *Int. J. Mater. Res.* **2005**, *96*, 566.
[85] V. Maier, A. Hohenwarter, R. Pippan, D. Kiener, *Scr. Mater.* **2015**, *106*, 42.
[86] T. G. Nieh, J. Wadsworth, *Mater. Sci. Eng. A* **1997**, *239–240*, 88.
[87] R. B. Figueiredo, T. G. Langdon, *J. Mater. Res. Technol.* **2021**, *14*, 137.
[88] M. Kawasaki, R. B. Figueiredo, T. G. Langdon, *Adv. Eng. Mater.* **2016**, *18*, 127.
[89] Y. M. Wang, A. V. Hamza, E. Ma, *Acta Mater.* **2006**, *54*, 2715.
[90] O. Renk, V. Maier-kiener, C. Motz, J. Eckert, D. Kiener, R. Pippan, *Materialia* **2021**, *15*, 101020.
[91] O. Renk, V. Maier-Kiener, I. Issa, J. H. Li, D. Kiener, R. Pippan, *Acta Mater.* **2019**, *165*, 409.
[92] A. Bachmaier, J. Schmauch, H. Aboulfadl, A. Verch, C. Motz, *Acta Mater.* **2016**, *115*, 333.
[93] A. Zhilyaev, G. Nurislamova, B.-K. Kim, M. Baró, J. Szpunar, T. Langdon, *Acta Mater.* **2003**, *51*, 753.
[94] S. Berg, D. Kutra, T. Kroeger, C. N. Straehle, B. X. Kausler, C. Haubold, M. Schiegg, J. Ales, T. Beier, M. Rudy, K. Eren, J. I. Cervantes, B. Xu, F. Beuttenmueller, A. Wolny, C. Zhang, U. Koethe, F. A. Hamprecht, A. Kreshuk, *Nat. Methods* **2019**, *16*, 1226.
[95] J. Schindelin, I. Arganda-Carreras, E. Frise, V. Kaynig, M. Longair, T. Pietzsch, S. Preibisch, C. Rueden, S. Saalfeld, B. Schmid, J.-Y. Tinevez, D. J. White, V. Hartenstein, K. Eliceiri, P. Tomancak, A. Cardona, *Nat. Methods* **2012**, *9*, 676.
[96] J. Brocher, *biovoxxel/BioVoxxel-Toolbox: BioVoxxel Toolbox (v2.5.3)*, Zenodo **2022**, https://doi.org/10.5281/zenodo.5986130.
[97] G. Bradski, *Dr. Dobb's J. Softw. Tools* **2000**, *120*, 122.

[98] S. van der Walt, J. L. Schönberger, J. Nunez-Iglesias, F. Boulogne, J. D. Warner, N. Yager, E. Gouillart, T. Yu, *PeerJ* **2014**, *2*, 453.
[99] P. Virtanen, R. Gommers, T. E. Oliphant, M. Haberland, T. Reddy, D. Cournapeau, E. Burovski, P. Peterson, W. Weckesser, J. Bright, S. J. van der Walt, M. Brett, J. Wilson, K. J. Millman, N. Mayorov, A. R. J. Nelson, E. Jones, R. Kern, E. Larson, C. J. Carey, Y. Feng, E.W. Moore, J. VanderPlas, D. Laxalde, J. Perktold, R. Cimrman, I. Henriksen, E. A. Quintero, C. R. Harris, A. M. Archibald, A. H. Ribeiro, F. Pedregosa, P. van Mulbregt, SciPy 1.0 Contributors, *Nat. Methods* **2020**, *17*, 261.

